

## Supporting Information

### Aligned Cobalt-Based Co@CoO<sub>x</sub> Nanostructures for Efficient Electrocatalytic Water Oxidation

Jing Qi,<sup>a</sup> Wei Zhang <sup>\*a</sup> and Rui Cao <sup>\*a,b</sup>

<sup>a</sup>School of Chemistry and Chemical Engineering, Shaanxi Normal University, Xi'an 710119, China

<sup>b</sup>Department of Chemistry, Renmin University of China, Beijing 100872, China

<sup>\*</sup>Correspondence to: zw@snnu.edu.cn; ruicao@ruc.edu.cn

## **General materials**

All chemicals, including Co(OAc)<sub>2</sub>·4H<sub>2</sub>O (99.999%, Alfa), diethyl oxalate (99%, Acros), sodium oxalate (99.8%, Sinopharm Chemicals), ethanol (99.5%, Sigma-Aldrich), KOH (98%, Sinopharm Chemicals), Ir/C (20 wt% of Ir, Premetek Co.) and Nafion (5 wt%, DuPont) were purchased from commercial suppliers and used without further purification. Milli-Q water of 18.2 MΩ·cm was used in all experiments.

## **Synthesis of materials**

In a typical synthesis of the CoC<sub>2</sub>O<sub>4</sub> nanoplates, Co(OAc)<sub>2</sub>·4H<sub>2</sub>O (1 mmol) was first dissolved in ethanol (25 mL) from 3 min of ultrasonication. Then, diethyl oxalate (10 mmol) was added to the solution. The mixture was then transferred into a Teflon-lined stainless steel autoclave with a volume capacity of 100 ml. The solvothermal reaction was subsequently conducted at 100 °C for 6 h. The solids were collected by centrifugation and washed with deionized water and ethanol thoroughly. The obtained solids were then dried in an oven at 60 °C overnight. The dried solids were subjected to further thermal treatment at different temperatures with a heating rate of 2 °C/min in a tube furnace under an Ar atmosphere. Cobalt metal nanoparticles were typically obtained after thermal treatment at 400 °C for 3 h.

## **Physical characterization**

Powder X-ray diffraction (XRD) patterns of the solids were recorded on a X-ray

diffractometer (Rigaku D/Max2550VB+/PC, Cu K $\alpha$ ,  $\lambda = 1.5406 \text{ \AA}$ , 40 kV and 100 mA).

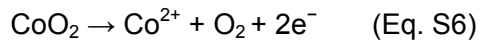
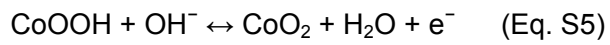
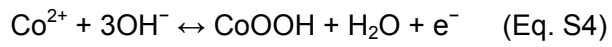
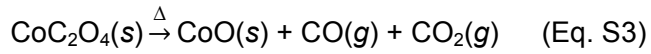
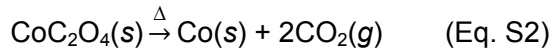
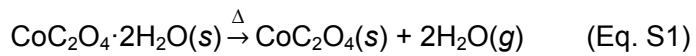
Infrared spectra (IR) were recorded on an IR spectrometer (Bruker, Tensor27) using a standard KBr pellet technique. Raman spectra were measured using a Renishaw inVia confocal Raman microscope with the excitation laser line at 532 nm. Thermogravimetric analysis (TGA) was carried out by heating the dry powder sample at a rate of  $5 \text{ }^{\circ}\text{C min}^{-1}$  with nitrogen flow at  $100 \text{ mL min}^{-1}$  over  $25 \text{ }^{\circ}\text{C}$  to  $800 \text{ }^{\circ}\text{C}$  in a TA Instruments SDT Q600. Derivative thermogravimetry (DTG) result was obtained based on the TGA data. The morphologies of the samples were observed on a Hitachi SU8020 cold-emission field emission scanning electron microscope (FESEM) with an accelerating voltage of 1 kV and a transmission electron microscopy (TEM, FEI, Tecnai G2 F20) with an accelerating voltage of 200 kV. The high resolution lattice image was acquired on the TEM. Energy-dispersive X-ray analysis (EDX) and the elemental mappings were conducted on an AMETEK Materials Analysis EDX equipped on the TEM. The samples were dispersed and loaded on carbon-coated copper grids for TEM analysis. The N<sub>2</sub> gas sorption isotherm and pore size distribution were measured on a Micromeritics ASAP 2020 at 77 K. The X-ray photoelectron spectroscopy (XPS) analysis of the samples was carried out on a Kratos AXIS ULTRA XPS. Monochromatic Al K $\alpha$  X-ray ( $h\nu = 1486.6 \text{ eV}$ ) was employed for analysis with photoelectron take-off angle of  $90^{\circ}$  with respect to surface plane. Correction of the binding energy was carried out using C 1s peak at 284.6 eV arising from the adventitious hydrocarbon. The surface content of CoO was analyzed by a H<sub>2</sub> temperature-programmed reduction (H<sub>2</sub>-TPR) method. The samples were loaded

on ITO electrodes and put into a quartz tube equipped on a chemisorption analyzer (AutoChem II 2920, Micromeritics). The tube line was degassed with Ar for half an hour under room temperature. It was then pretreated under Ar from room temperature to 300 °C at a heating rate of 10 °C/min and was kept at 300 °C for 2 h to convert the surface hydroxides into oxides. The system was then cooled to room temperature and kept for half an hour under Ar. Subsequently, the gas flow was switched to H<sub>2</sub>/Ar (10 vol%), and the furnace was heated to 500 °C at 10 °C/min. All the gas flows were 30 mL/min. The consumed H<sub>2</sub> amount was determined by an on line thermal conductivity detector (TCD). Pure CoO standard samples on ITO electrodes were referred to obtain the calibration line based on the same temperature program.

### **Electrochemical studies**

All electrochemical experiments were carried out using a CH Instruments (CHI 660E Electrochemical Analyzer) at 20 °C. Linear sweep voltammograms (LSV) and cyclic voltammograms (CVs) were conducted in 15 mL of 1 M KOH aqueous solution using a conventional three-electrode configuration with a glassy carbon (GC, 0.07 cm<sup>2</sup>) electrode as the working electrode, saturated Ag/AgCl as the reference electrode, and Pt wire as the auxiliary electrode. The scan rates were 50 mV s<sup>-1</sup>. The working electrode was prepared through a drop-casting method. Typically, 4 mg of sample and 30 µL of Nafion solution (5 wt%, DuPont) were dispersed in 1 mL of water-ethanol solution at volume ratio of 2:1 by ultrasonication for 30 min to form a homogeneous suspension.

Then 5  $\mu$ L of the mixture was loaded onto the GC electrode. Compensation for iR drop was used for all LSVs and CVs. All potentials were reported versus the reversible hydrogen electrode (RHE) based on the equation:  $E_{\text{RHE}} = E_{\text{Ag/AgCl}} + (0.197 + 0.0591 \times \text{pH})$ . Current-potential data for Tafel plots were acquired by LSV measurements for oxygen evolution reaction (OER) currents at a scan rate of 1 mV s<sup>-1</sup> with iR compensation. Controlled potential electrolysis (CPE) was measured on indium tin oxide (ITO, 0.25 cm<sup>2</sup>) electrode at 1.55 V in a fritted cell without iR drop compensation. The amount of the evolved oxygen was measured by an Ocean Optics FOXY probe. The mass loading of the catalysts is 0.32 mg cm<sup>-2</sup>. The electrochemical impedance spectroscopy (EIS) was recorded on an ITO electrode over a frequency range from 0.1 Hz to 1 MHz at the amplitude of the sinusoidal voltage of 5 mV under 1.55 V.



$$\left( \frac{\partial E}{\partial pH} \right)_j = - \left( \frac{\partial E}{\partial \log(j)} \right)_{pH} \left( \frac{\partial \log(j)}{\partial pH} \right)_E \quad (\text{Eq. S7})$$

**Tab. S1** The comparison of the OER performances between the Co@CoO<sub>x</sub> nanoparticles and some Co-based electrocatalysts in recent publications.

Catalyst	Substrate	Electrolyte	Overpotential @10 mA cm <sup>-2</sup> (mV)	Reference
<b>Co@CoO<sub>x</sub> NP</b>	<b>GC</b>	<b>1 M KOH</b>	<b>289</b>	<b>This work</b>
Co-P film	Cu foil	1 M KOH	345	<i>Angew. Chem. Int. Ed.</i> , 2015, <b>54</b> , 6251
CoCo LDH	GC	1 M KOH	350	<i>Nat. Commun.</i> , 2014, <b>5</b> , 4477
N-CG-CoO	GC	1 M KOH	340	<i>Energy Environ. Sci.</i> , 2014, <b>7</b> , 609
Co <sub>x</sub> O <sub>y</sub> /NC	GC	0.1 M KOH	430	<i>Angew. Chem. Int. Ed.</i> , 2014, <b>53</b> , 8508
NiCo LDH	Carbon paper	1 M KOH	367	<i>Nano Lett.</i> , 2015, <b>15</b> , 1421
Co <sub>3</sub> O <sub>4</sub>	FTO	1 M NaOH	376	<i>Adv. Energy Mater.</i> , 2016, <b>6</b> , 1600697
Ni-Co-mixed oxide cages	GC	1 M KOH	380	<i>Adv. Mater.</i> , 2016, <b>28</b> , 4601
MnCoP NP	GC	1 M KOH	330	<i>J. Am. Chem. Soc.</i> , 2016, <b>138</b> , 4006
Co-B <sub>x</sub> /Graphene	GC	1 M KOH	290	<i>Angew. Chem. Int. Ed.</i> , 2016, <b>55</b> , 2488
CoSe <sub>2</sub> NS	GC	0.1 M KOH	320	<i>J. Am. Chem. Soc.</i> , 2014, <b>136</b> , 15670
NiCoP/rGO	Carbon paper	1 M KOH	270	<i>Adv. Funct. Mater.</i> , 2016, <b>26</b> , 6785
CoO <sub>x</sub> @NC	Ni foam	1 M KOH	260	<i>J. Am. Chem. Soc.</i> , 2015, <b>137</b> , 2688
CoP NS/Carbon	GC	1 M KOH	277	<i>Green Chem.</i> , 2016, <b>18</b> , 2287
CoP	GC	1 M KOH	320	<i>ACS Catal.</i> , 2015, <b>5</b> , 6874
Co <sub>3</sub> O <sub>4</sub> nanotubes	GC	0.1 M KOH	390	<i>Angew. Chem. Int. Ed.</i> , 2016, <b>55</b> , 9055

NP: nanoparticles; LDH: layered double hydroxide; NC: N-doped carbon; NS: nanosheets; rGO: reduced graphene oxide; GC: glassy carbon electrode; FTO: F-doped tin oxide electrode.

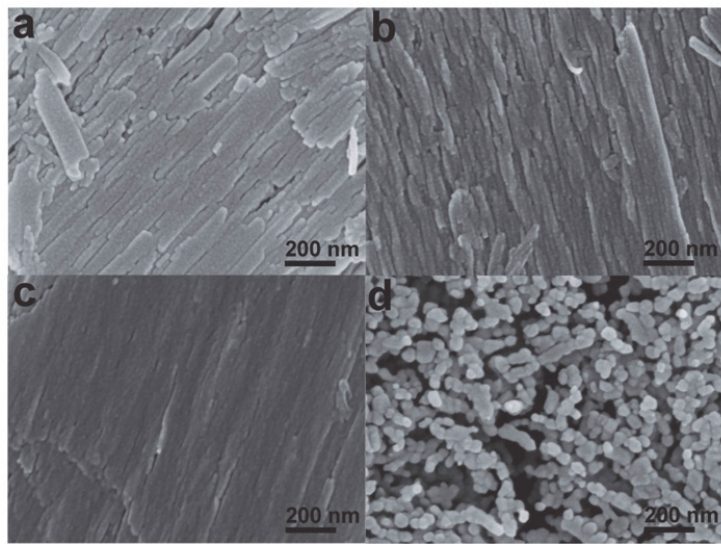


Fig. S1 The SEM images of the solvothermal-prepared Co-based materials after the thermal treatment in Ar at different temperatures: (a) RT, (b) 200 °C, (c) 300 °C, and (d) 500 °C.

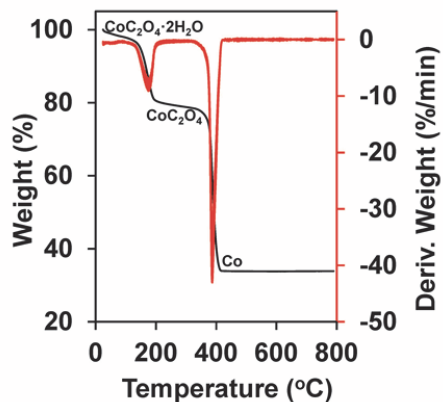


Fig. S2 The TGA (black) and DTG (red) curves of the solvothermal-prepared  $\text{CoC}_2\text{O}_4\cdot 2\text{H}_2\text{O}$  material under a  $\text{N}_2$  flow, indicating the loss of the lattice water at 172 °C and the decomposition to the Co metal at 385 °C.

The TGA was carried out to identify the weight loss of the  $\text{CoC}_2\text{O}_4\cdot 2\text{H}_2\text{O}$  material under an inert atmosphere. The gradual weight loss before 120 °C is from the evaporation of the adsorbed water in the material. There are two dominant weight losses at 172 and 385 °C, which are corresponding to the dehydration of the lattice water of  $\text{CoC}_2\text{O}_4\cdot 2\text{H}_2\text{O}$  and the subsequent decomposition of  $\text{CoC}_2\text{O}_4$  to Co, respectively. The weight percentages of the residues are in good agreement with the above-mentioned conversions.

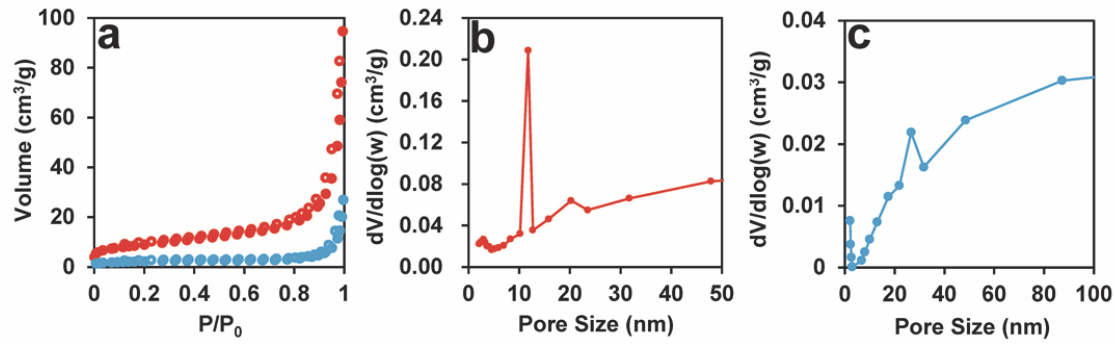


Fig. S3 (a) The adsorption-desorption isotherms and (b, c) the pore size distributions of the cobalt oxalate (red) and the pyrolysis-derived cobalt metal (blue).

Physical characterizations of the  $\text{CoC}_2\text{O}_4 \cdot 2\text{H}_2\text{O}$  material before and after its conversion to the Co metal were performed by the  $\text{N}_2$  sorption. The sorption results indicate similar type-II isotherms with rapid rises at  $P/P_0 > 0.8$ , which accompany weak hysteresis loops. The pyrolysis of the oxalate material decreased its BET surface area from 31.9 to  $7.9 \text{ m}^2 \text{ g}^{-1}$ . The pore size distribution of the oxalate displays a sharp peak with pore size at approximately 10~12 nm. Whereas the cobalt metal exhibits a successive increase of the pore volume at increased pore sizes, which is a typical phenomenon caused by the packing of nanoparticles, as also illustrated in the SEM and TEM images (Fig. 2).

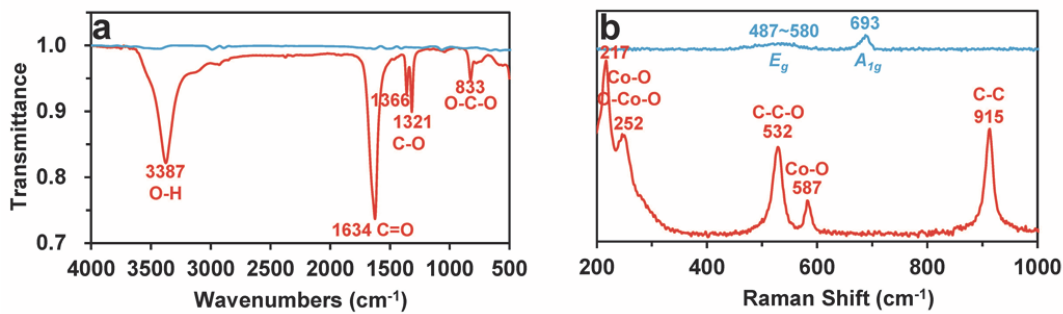


Fig. S4 (a) The infrared spectra and (b) the Raman spectra of the cobalt oxalate (red) and the pyrolysis-derived cobalt metal (blue).

For the IR spectrum, the strong single peak at  $1634 \text{ cm}^{-1}$  can be assigned to the C=O stretching vibration. The two proximate peaks at  $1366$  and  $1321 \text{ cm}^{-1}$  are attributed to the C–O asymmetric and symmetric vibrations, respectively. The small peak at  $833 \text{ cm}^{-1}$  is due to the O–C–O vibration.<sup>1</sup> The C–C stretching, which is IR-inactive, is demonstrated by the Raman spectrum with a sharp peak at  $915 \text{ cm}^{-1}$ . Another two Raman peaks at  $587$  and  $532 \text{ cm}^{-1}$  are from the Co–O stretching (or O–Co–O ring deformation) and the C–C–O bending modes, respectively. The Raman shifts bellow  $300 \text{ cm}^{-1}$  can also be determined as the Co–O stretching and O–Co–O ring bending modes.<sup>2</sup> There are hardly peaks from the IR analysis of the cobalt metal, and the Raman analysis indicates two weak peaks at  $487\text{--}580$  and  $693 \text{ cm}^{-1}$ . These two peaks are in good agreement with the signals determined from pure CoO material reported in literatures.<sup>3</sup> The formation of a thin layer of oxides on the cobalt metal surface after its exposure to air is reasonable, which is also supported by the XPS analyses (Fig. S5).

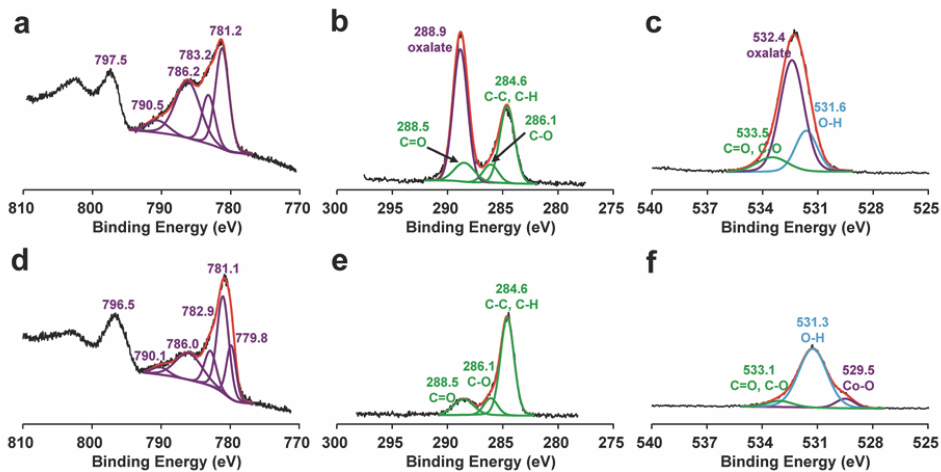


Fig. S5 The XPS analyses of (a-c) the cobalt oxalate and (d-f) the pyrolysis-derived cobalt metal near the (a, d) Co 2p, (b, e) C 1s and (c, f) O 1s binding energy regions.

The Co 2p<sub>3/2</sub> narrow-scan spectrum of the oxalate is fitted into two main peaks at 781.2 and 783.2 eV (a). Two fitted satellite peaks are also included in the Co 2p<sub>3/2</sub> spectrum with a broad one at 786.2 eV and a small one at 790.5 eV. The binding energies of the two main peaks and the broad satellite peak are consistent with the Co 2p<sub>3/2</sub> spectra of many inorganic Co<sup>II</sup>-containing materials with unpaired Co 3d electrons.<sup>4</sup> The C 1s spectrum indicates a strong peak at 288.9 eV, which is corresponding to the carbon from oxalate anions (b, purple line). The signal of the adventitious carbon is also fitted, as illustrated by the green lines. Similarly, the O 1s spectrum can also be fitted to display the strong signal of oxalate anions at 532.4 eV. A peak at 531.6 eV, which is from the hydroxide group, is also present (c). According to the XRD analysis, the cobalt metal is prepared after the pyrolysis of the oxalate. The XPS analysis of the cobalt metal surface

for the Co 2p, C 1s and O1s spectra are provided in (d-f). Compared with the Co 2p signal of the oxalate precursor, the Co 2p signal of the cobalt metal has the following differences. First, a peak with a lower binding energy of 779.8 eV can be fitted in the Co 2p<sub>3/2</sub> core photoelectron line. Second, the Co 2p<sub>3/2</sub> satellite peak is weakened. Third, the position of the Co 2p<sub>1/2</sub> main peak is lowered from 797.5 eV to 796.5 eV. All of these findings indicate the presence of the Co<sup>0</sup> species.<sup>5</sup> However, the Co<sup>II</sup> species is also present on the surface of the cobalt metal, as also supported by the surface Raman analysis (Fig. S4). The C 1s spectrum from the cobalt metal is consistent with that of the typical adventitious carbon, and the oxalate signal is totally disappeared. The O 1s spectrum indicates a small peak of the cobalt oxide and a dominant peak of the surface hydroxyl adducts.<sup>4a</sup>

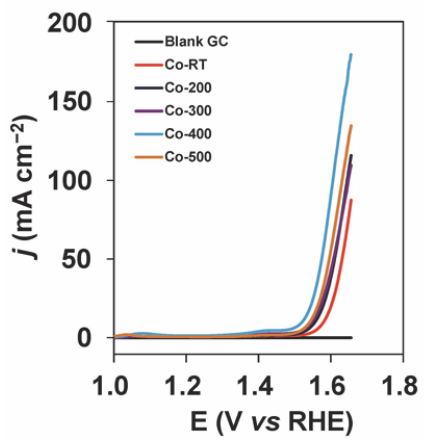


Fig. S6 The LSV polarization curves of the Co-based samples prepared at different pyrolysis temperatures for OER in a 1 M KOH aqueous solution.

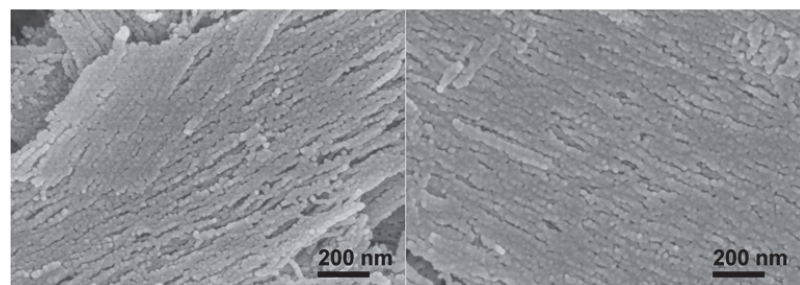


Fig. S7 The SEM images of the aligned Co metal nanoparticles after one week of storage in dry conditions.

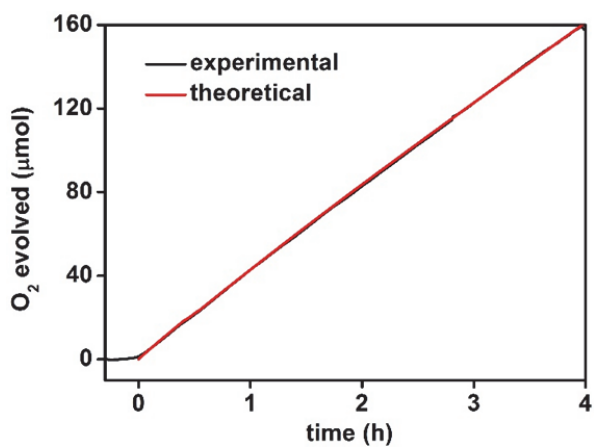


Fig. S8 The theoretical and experimental amounts of the evolved oxygen gas during the controlled potential electrolysis of the Co/CoO<sub>x</sub> catalyst for OER at 1.55 V vs RHE. The Faradaic efficiency is close to 100%.

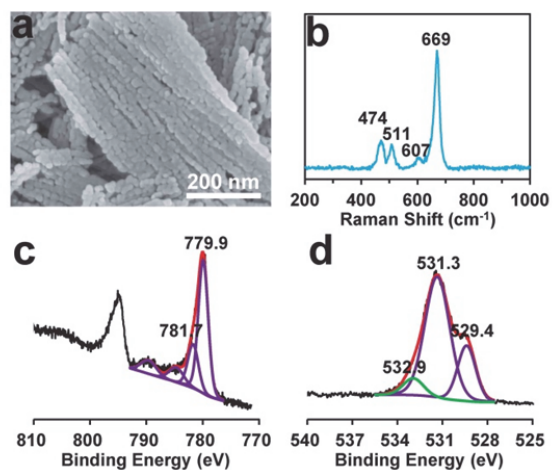


Fig. S9 (a) The SEM image, (b) the Raman spectrum, and (c) the Co 2p and (d) O 1s XPS narrow scan spectra of the cobalt nanoparticles after 24 h of electrolysis at 1.55 V for OER.

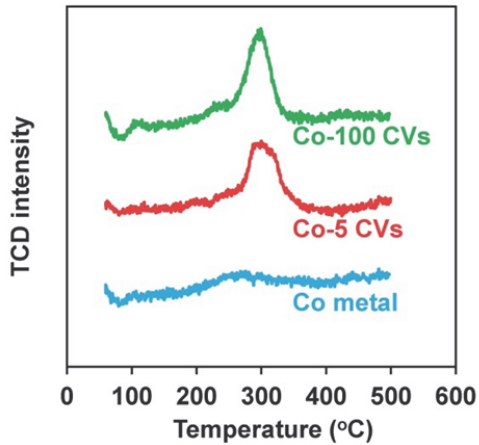


Fig. S10 The H<sub>2</sub>-TPR profiles of the as-prepared Co metals and the Co-metal after 5 and 100 cycles of OER test.

We investigated the Co oxide contents in the as-prepared Co metal, and the Co-metal after 5 and 100 cycles of OER test by H<sub>2</sub> temperature programmed reduction (H<sub>2</sub>-TPR) method. The Co oxide content on the surface of the as-prepared metal nanoparticles is negligible as no obvious TPR peak is observed. After 5 and 100 cycles of CV tests for OER, the surface cobalt oxide contents on the Co metals are determined to be 18.5 and 16.1 wt%, respectively. This information is consistent with the conclusions that the polarization generated surface oxides as active OER species, and that the content of the surface oxides did not increase under prolonged OER test due to the surface passivation from the quickly in-situ formed oxides.

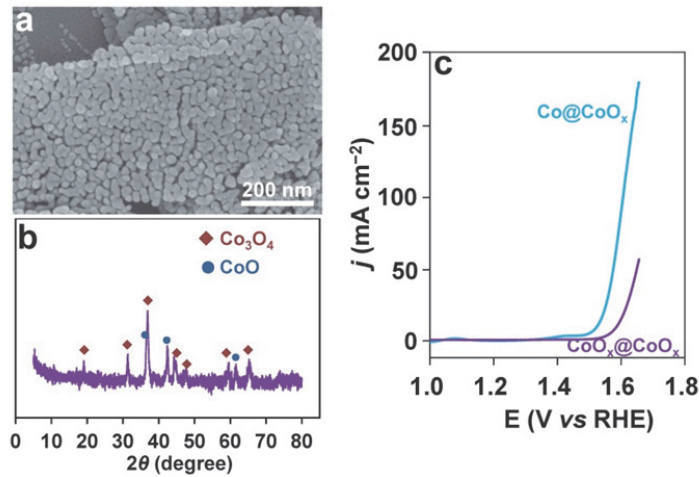


Fig. S11 The SEM image (a) and XRD pattern (b) of the sample prepared by calcination of the Co metal sample in air at 300 °C for 2 h; (c) the OER performances of the polarized Co metal (blue) and Co oxides (purple).

To get a (semi)quantitative argument of the activity enhancement by the bulk conductivity, a sample was synthesized by the calcination of the Co metal sample in air at 300 °C for 2 h and tested for OER. The SEM image showed the preserved 2D-alignment of nanoparticles, and the XRD pattern of this new sample indicates the cobalt oxide phases. The  $\text{Co}@\text{CoO}_x$  sample showed superior OER activity than the  $\text{CoO}_x@\text{CoO}_x$  sample, indicating the activity enhancement resulted from the bulk conductivity.

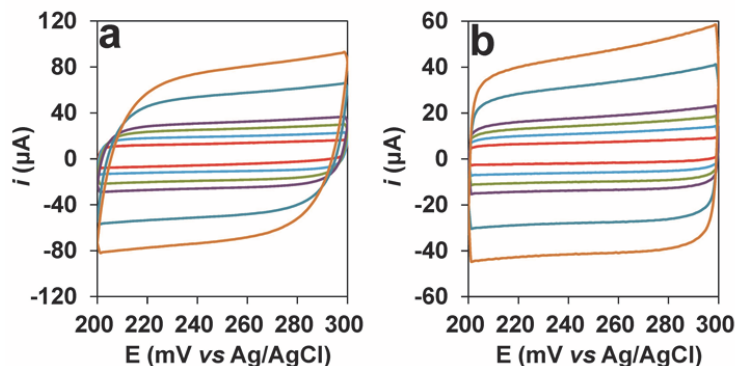


Fig. S12 The charging currents of (a) the cobalt oxalate and (b) the pyrolysis-derived cobalt metal recorded in the non-Faradaic potential region (200~300 mV *vs* Ag/AgCl) at scan rates of 5, 10, 15, 20, 40 and 60  $\text{mV s}^{-1}$  (increasing capacitive currents).

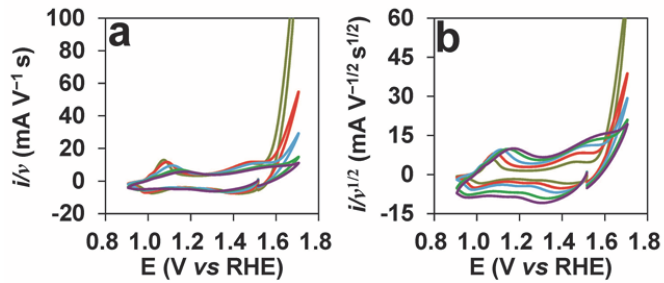


Fig. S13 The CV (a)  $i/v$  and (b)  $i/(v^{1/2})$  responses to potentials of the cobalt metal electrocatalyst at different scan rates: 0.2 (olive), 0.5 (red), 1 (blue), 2 (green), and 3 (purple) V s $^{-1}$ .

## References

- 1 D. Wang, Q. Wang and T. Wang, *Inorg. Chem.*, 2011, **50**, 6482.
- 2 R. L. Frost and M. L. Weier, *J. Raman Spectrosc.*, 2003, **34**, 776.
- 3 a) H. C. Choi, Y. M. Jung, I. Noda and S. B. Kim, *J. Phys. Chem. B*, 2003, **107**, 5806;  
b) C.-W. Tang, C.-B. Wang and S.-H. Chien, *Thermochim. Acta*, 2008, 473, 68.
- 4 a) J. Yang, H. Liu, W. N. Martens and R. L. Frost, *J. Phys. Chem. C*, 2010, **114**, 111;  
b) H. Chen, Y. Zhang, J. Yang, Z. Dai, N. Fu, W. Huang and X. Dong, *J. Mater. Chem. A*, 2015, **3**, 20690.
- 5 M. C. Biesinger, B. P. Payne, A. P. Grosvenor, L. W. M. Lau, A. R. Gerson and R. S. C. Smart, *Appl. Surf. Sci.*, 2011, **257**, 2717.